



**HAL**  
open science

## Sub-pixel detection of laser-induced damage and its growth on fused silica optics using registration residuals

Guillaume Hallo, Chloé Lacombe, Romain Parreault, Nadja Roquin, Thierry Donval, Laurent Lamaignère, Jérôme Néauport, François Hild

► **To cite this version:**

Guillaume Hallo, Chloé Lacombe, Romain Parreault, Nadja Roquin, Thierry Donval, et al.. Sub-pixel detection of laser-induced damage and its growth on fused silica optics using registration residuals. *Optics Express*, 2021, 29 (22), pp.35820-35836. 10.1364/oe.433862 . hal-03491141

**HAL Id: hal-03491141**

**<https://hal.science/hal-03491141v1>**

Submitted on 17 Dec 2021

**HAL** is a multi-disciplinary open access archive for the deposit and dissemination of scientific research documents, whether they are published or not. The documents may come from teaching and research institutions in France or abroad, or from public or private research centers.

L'archive ouverte pluridisciplinaire **HAL**, est destinée au dépôt et à la diffusion de documents scientifiques de niveau recherche, publiés ou non, émanant des établissements d'enseignement et de recherche français ou étrangers, des laboratoires publics ou privés.



# Sub-pixel detection of laser-induced damage and its growth on fused silica optics using registration residuals

GUILLAUME HALLO,<sup>1,2,\*</sup>  CHLOÉ LACOMBE,<sup>1</sup> ROMAIN PARREAULT,<sup>1</sup> NADJA ROQUIN,<sup>1</sup> THIERRY DONVAL,<sup>1</sup> LAURENT LAMAIGNÈRE,<sup>1</sup> JÉRÔME NÉAUPORT,<sup>1</sup>  AND FRANÇOIS HILD<sup>2</sup> 

<sup>1</sup>CEA, CESTA, F- 33116, Le Barp, France

<sup>2</sup>Université Paris-Saclay, ENS Paris-Saclay, CNRS, LMT - Laboratoire de Mécanique et Technologie, 91190 Gif-sur-Yvette, France

\*guillaume.hallo@cea.fr

**Abstract:** Fused silica optics are key components to manipulate high energy Inertial Confinement Fusion (ICF) laser beams but their optical properties can be degraded by laser-induced damage. The detection of laser damage sites is of major importance. The challenge is to monitor damage initiation and growth at sub-pixel scale with highly sensitive measurements. The damage diameter is a widely used indicator to quantify damage growth but its accuracy is strongly dependent on the available image resolution. More recently, it was shown that registration residual maps (*i.e.*, gray level differences between two registered images) could also be used to monitor laser-induced damage. In this paper, the performance of both indicators are compared to detect laser damage initiation and growth at high and low image resolutions thanks to a highly instrumented laser setup. The results prove that registration residual maps are more efficient to detect sub-pixel laser damage growth than diameter measurements at a given image resolution. The registration residual maps are therefore a powerful indicator for monitoring laser-induced damage initiation and growth at sub-pixel scale either for laser damage metrology setups, for high energy laser facilities, or other situations where damage is suspected to occur. The accuracy of (laser-induced) damage laws may also be improved thanks to this tool.

© 2021 Optical Society of America under the terms of the [OSA Open Access Publishing Agreement](#)

## 1. Introduction

The optics of high energy Inertial Confinement Fusion (ICF) laser facilities suffer from laser-induced damage. Once a damage site initiates, it grows after each ultraviolet laser shot since the ultraviolet energy is greater than the growth threshold [1]. Due to the presence of damage sites on final fused silica components, the available laser energy is limited for each experiment. Some techniques have been developed to limit damage growth such as locally reducing the laser energy under the growth threshold by shadowing [2] or using CO<sub>2</sub> laser optics mitigation [3,4]. However, optics mitigation at the Laser MegaJoule (LMJ) facility is effective only if the damage site diameter is less than 700 μm, and if early damage growth is measurable. Hence, the objective is to detect laser damage sites before they reach sizes of about 100 μm [2,5]. This physical size represents about one pixel for observation systems of high energy laser installations such as Final Optics Damage Inspection (FODI) at the National Ignition Facility (NIF) [6] and ShenGuang-III (SG-III) [7], or the Chamber Center Diagnostic Module (MDCC [2,8]) of the LMJ facility [8]. Consequently, sub-pixel damage detection is needed on such final optics. The observed final optics at NIF are the vacuum windows, the second and third harmonic generator crystals, the final focusing lens and the main debris shield [6] whereas only the vacuum windows and the focusing gratings are observed at LMJ [2].

In order to monitor laser damage, different methods have been developed to detect its growth as soon as possible without removing the component. It was proposed to detect potential damage sites using an algorithm based on the analysis of the Local Area Signal-to-Noise Ratio (LASNR) for each pixel of each image [9]. This algorithm is widely used at NIF and LMJ to detect damage sites on final optics. An algorithm based on local area signal strength and 2D histogram was then applied to damage detection [10]. These algorithms are deemed efficient for early detection of damage sites. NIF announced the detection of sites whose diameter was at least 30  $\mu\text{m}$ , which is three tenth of the resolution of FODI images by using the integrated signal captured from a laser-induced damage site to calculate the area and size of small sites [6].

However, due to apparent motions and lighting and background variations from one image to another, it is difficult to perform an efficient metrology of damage growth. These fluctuations modify the gray levels (*i.e.*, image intensity) of each pixel between successive acquisitions. Before any image correction, the registration residual map, which is the gray level difference between a reference image and an image of the same optics acquired after some laser shots, is a function of apparent motions, lighting and background variations, damage growth and acquisition noise. A method to correct for motions as well as lighting and background variations was recently developed [8]. The corrections, which consist in spatial image registrations based on Digital Image Correlation principles [11] coupled with brightness and contrast corrections [12], make it possible to compare gray level variations of each pixel from one image to another. This technique is widely used in solid mechanics in order to monitor mechanical tests [11,13,14], to extract useful data for damage detection and quantification [15,16]. In the present case, the first step is the measurement of the displacement field between a reference image and a set of images acquired after each laser shot. The second step consists in correcting for low order gray level variations that are due to lighting and background variations. After these corrections are carried out, the registration residual map becomes a function of damage growth and acquisition noise only. Pixels in the registration residual map that have higher gray levels than the noise level may be attributed to damage initiation or growth. This method may enable for earlier detection of potential damage sites than using the so-called LASNR algorithm.

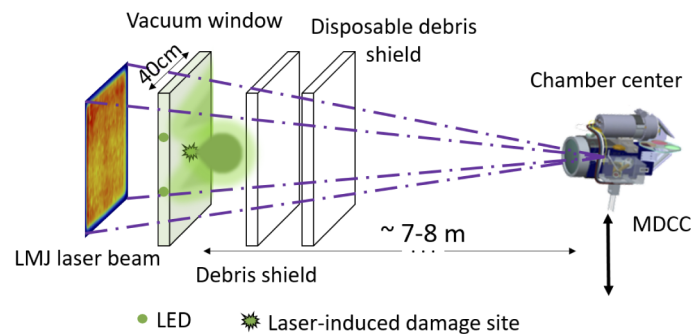
The first aim of this paper is to demonstrate the effectiveness of image registration with sub-pixel resolution performing registrations on images typical of final optics. The second objective is to estimate the smallest damage diameter variation that is noticeable and detectable on images with a 100  $\mu\text{m}/\text{pixel}$  resolution *via* two indicators: the measured diameter of a damage site and the registration residual map. It is proposed to use high resolution images (*i.e.*, 6.5  $\mu\text{m}/\text{pixel}$ ) of a fused silica component that can be down-sampled to obtain similar low resolution images (*i.e.*, 100  $\mu\text{m}/\text{pixel}$ ) of optics acquired at LMJ, NIF and SG-III. These high resolution images were acquired on a highly instrumented experimental laser setup (*i.e.*, MELBA [17–21]) designed to reproduce LMJ conditions of laser shots at the wavelength of 351 nm followed by image acquisitions.

The MELBA setup is described in Section 2. The noise level was estimated with and without displacements between acquisitions at high and low resolutions in Section 3. Sample and camera motions were applied in order to validate the registration algorithm based on digital image correlation principles on high and low resolution images (Section 4). Laser damage sites were initiated on the sample to estimate the smallest damage site visible at both resolutions (Section 5.1). One hundred laser shots were used to grow initiated laser damage sites. Detection thresholds of damage growth were then estimated at both resolutions in Section 5.2. The present paper is based on LMJ-like data but it is believed that the advantages of the method are valid for detecting and monitoring laser damage growth for laser damage metrology setup, for high energy laser facilities with needs of sub-pixel resolution, and possibly other configurations in which damage is suspected to occur.

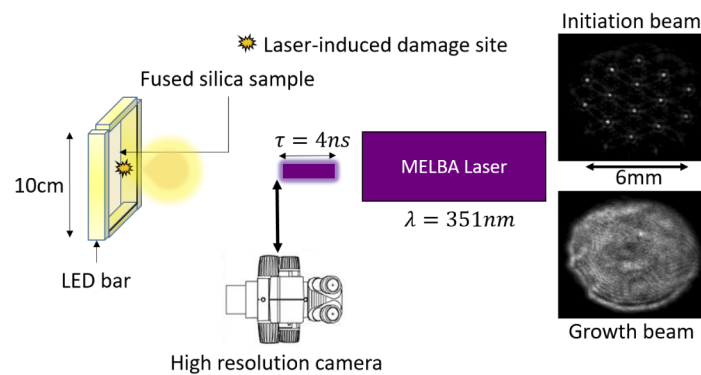
## 2. Experimental setup

At the LMJ facility, images of optics are acquired by a camera, with the so-called MDCC system [2,8], after each laser shot. The observation system is composed of two green LEDs placed near one edge of a vacuum window. Lighting provided by LEDs enters into the optics and illuminates rear and front sides of the component. Laser damage sites scatter light. A part of the scattered light from damage is collected by the MDCC camera focused on the front side of the vacuum window. A vacuum window is a 40 cm  $\times$  40 cm fused silica optics with 34 mm thickness. The MDCC setup is shown in Fig. 1(a). The operating sequence is composed of three parts:

- The 35 cm  $\times$  35 cm ultraviolet nanosecond laser beam irradiates the vacuum window with fluences ranging from 1 to 8 J/cm<sup>2</sup>. At these fluences, damage initiation and growth may occur [1].
- The MDCC module is placed at the center of the experiment chamber and oriented toward the vacuum window. The lighting system is switched on. Laser damage sites are visible. Images of the optics are acquired at 100  $\mu$ m/pixel resolution.
- The lighting system is switched off. Background images are acquired and subtracted from images of the optics. The MDCC module is removed from the experiment chamber.



(a)



(b)

**Fig. 1.** (a) MDCC image acquisition setup at LMJ with the path of the laser beam shown in purple dash-dotted line. (b) MELBA experimental setup with the spatial shape of two available nanosecond ultraviolet laser beams.

The characterization optical (MELBA) setup has been widely used to study laser damage initiation and growth in order to understand and quantify laser-induced damage as functions of laser parameters [18,20,21]. This highly instrumented setup was used herein to reproduce the MDCC operating sequence but with high resolution images (*i.e.*, 6.5  $\mu\text{m}/\text{pixel}$ ). MELBA is composed of a lighting system integrated to the sample holder, a high resolution camera that can be translated, and a nanosecond ultraviolet laser beam (Fig. 1(b)). The sample used for this experiment is a 10 cm  $\times$  10 cm fused silica component with 34 mm thickness.

Table 1 compares the characteristics of the MDCC acquisition setup with those obtained with the MELBA setup. Both setups provide dark field images of a fused silica component. The MELBA camera can be moved horizontally. The position of the focal plane can also be adjusted. The sample holder allows for the following displacements: translations (vertical and horizontal directions), and rotation about the vertical axis. The spatial resolution of the MELBA camera is 15 times higher than that of the MDCC camera. This high resolution allows damage site diameters to be assessed very accurately.

**Table 1. Characteristics of MDCC and MELBA setups.**

Set-up	MDCC	MELBA
<i>Lighting system</i>	2 green LEDs	4 LED bars
<i>Camera definition</i>	4096 $\times$ 4096 pixels	1392 $\times$ 1040 pixels
<i>Pixel depth</i>	16 bits	8 bits
<i>Image resolution</i>	100 $\mu\text{m}/\text{pixel}$	6.5 $\mu\text{m}/\text{pixel}$
<i>Imaged area</i>	409 mm $\times$ 409 mm	9 mm $\times$ 6.8 mm

In order to make LMJ vacuum window image registration possible, four fiducials were laser etched on each corner of the optics (in green boxes in Fig. 2(a)). These fiducials are craters made by ablation with a CO<sub>2</sub> laser on the front face of the optics. They are used by the registration algorithm to perform displacement corrections between successive image acquisitions [8]. To mimic fiducials on the MELBA silica sample, laser damage sites were initiated in each corner of the imaged area (Fig. 2(b)). Four different patterns make it possible to distinguish each corner of the image. The intensity of the lighting system and the camera exposure time were chosen so that the markers did not saturate the sensor. These markers have a similar purpose as the random black and white speckle (Fig. 2(c)) widely used in digital image correlation [11].

Two properties of the areas used for image registration purposes are summarized in Table 2. The mean image contrast is defined by

$$\sqrt{\langle \|\nabla I\|_2^2 \rangle} = \sqrt{\frac{1}{N_{pix}} \sum_{\mathbf{x}} \|\nabla I(\mathbf{x})\|_2^2}, \quad (1)$$

where  $N_{pix}$  is the number of pixels in the region of interest,  $\mathbf{x}$  the vector position of each considered pixel, and  $\|\bullet\|_2$  the L<sub>2</sub>-norm. In digital image correlation, it was shown that the standard displacement uncertainties are inversely proportional to the mean contrast [22]. Random (speckle) patterns are “image correlation friendly” as they usually cover the whole region of interest of the images to be registered, and provide high contrasts (Fig. 2(c)). On the contrary, the areas used for spatial registrations of the optics images cover a much smaller part of the images, and do not correspond to the analysis area for damage detection and quantification. They also provide a lower contrast. The MELBA markers have similar properties as LMJ fiducials. The effectiveness of sub-pixel registration for MDCC images was evaluated using MELBA images as both configurations were similar. Despite these degraded situations, it will be shown that image registration of such images was possible and effective (Section 4).

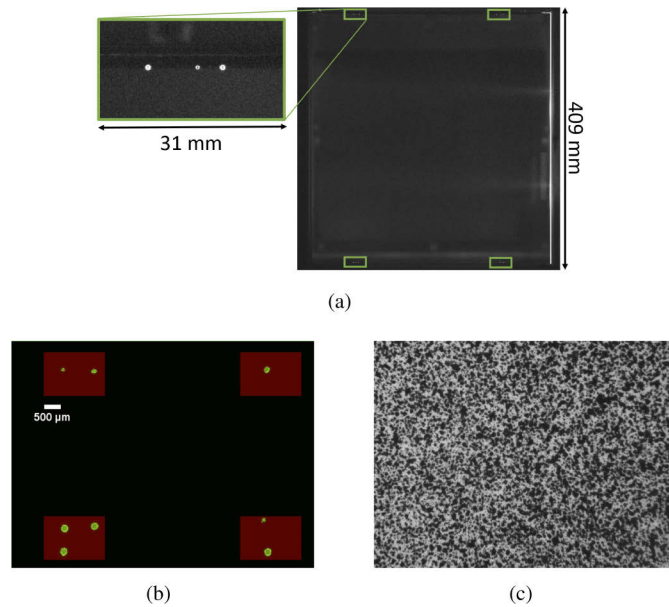


**Fig. 2.** (a) MDCC vacuum window image with fiducials in green boxes. (b) MELBA image of the silica sample with markers in green color inside red boxes. (c) Random black and white pattern.

**Table 2. Characteristics of areas and mean contrast used for image registration purposes: random black and white pattern, MELBA markers and LMJ fiducials (Fig. 2).**

	Random pattern	MELBA markers	LMJ fiducials
<i>Image area (percentage)</i>	100 %	15 %	1 %
$\sqrt{\langle \ \nabla I\ _2^2 \rangle}$ (gray level/pixel)	28	2.8	6.9

In order to compare the effectiveness of measured diameters and registration residuals to detect small damage growth at high and low image resolutions, nanosecond ultraviolet laser shots were performed on the fused silica component using the MELBA setup. Two configurations were used:

- Damage initiation configuration (in magenta in Fig. 3) – Before reaching the fused silica sample, the laser beam traversed an optical component composed of 19 phase rings in a hexagonal array that changes the fluence shape of the laser beam [19]. On the fused silica plane, the laser beam featured intense spots where fluences were locally about  $30 \text{ J/cm}^2$ . At these fluences, the probability of damage initiation tends toward unity [1,21,23].
- Damage growth configuration (in blue in Fig. 3) – The fluence shape of the laser beam was more uniform than in the previous configuration since phase rings were removed from the laser path. The mean fluences ranged from 1 to  $9 \text{ J/cm}^2$  during the growth step. The growth threshold fluence was measured at about  $5 \text{ J/cm}^2$  for a pulse duration of 4 ns [24]. The damage growth threshold was overcome using the MELBA damage growth configuration.

In both configurations, the pulse duration was 4 ns.

The results that will be reported in Sections 3 and 4 were obtained with no laser shot. The image of the fused silica sample contained only the registration markers. The results that will be reported in Section 5.1 were obtained by initiating laser damage sites with 3 laser shots in the

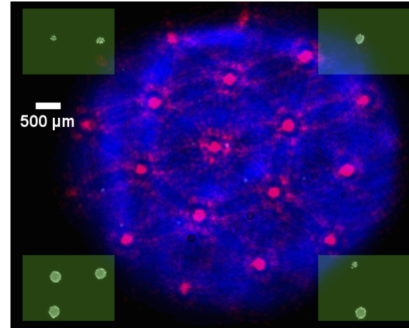


**Fig. 3.** Composite image depicting the observed area of the fused silica sample by the high resolution camera. Initiated laser markers are displayed in light green. The area used for image registration purposes is represented as green boxes. The damage initiation beam is shown in magenta. The damage growth beam is shown in blue.

MELBA damage initiation configuration. The objective was to estimate the smallest damage site detectable at 100  $\mu\text{m}/\text{pixel}$  resolution. The results that will be reported in Section 5.2 were obtained with one hundred laser shots in the damage growth configuration. The aim was to estimate the ability of the indicators to detect damage growth.

### 3. Uncertainty quantification

Since the MDCC is removed from the experiment chamber before each laser shot, it was necessary to quantify MELBA acquisition uncertainties with applied displacements between acquisitions. In order to estimate the minimum reachable registration residual level in the MELBA configuration, 100 images were acquired with no laser shot; 20 among them with no applied displacement. Consequently, the Root Mean Square (RMS) residual should be at the noise level if the positions of the camera and the sample holder were perfectly stable. This acquisition sequence with no displacement corresponds to images 0 to 19. Image 0 was considered as the reference. 80 images were acquired after a prescribed displacement and automatic return to the reference position of the camera between each acquisition. This second configuration with camera translations between acquisitions mimics the acquisition process at LMJ. If the mechanical return were perfect, the RMS residual should also be at the noise level. This sequence corresponds to images 20 to 99.

The image registration algorithm used herein is based on the gray level conservation hypothesis [11]

$$I_0(\mathbf{x}) = I_t(\mathbf{x} + \mathbf{u}(\mathbf{x})), \quad (2)$$

where  $I_0$  is the reference image,  $I_t$  the “deformed” image,  $\mathbf{x}$  the pixel position, and  $\mathbf{u}$  the sought displacement vector between the reference and deformed configurations. The aim of the registration procedure is to estimate the displacement field  $\mathbf{u}(\mathbf{x})$  that minimizes, over the four marker areas (green zones in Fig. 3), the  $L_2$  norm of the registration residual  $\rho$  defined as

$$\rho(\mathbf{x}) = I_0(\mathbf{x}) - I_t(\mathbf{x} + \mathbf{u}(\mathbf{x})). \quad (3)$$

The measured displacement field  $\mathbf{u}$  is written as a linear combination of in-plane horizontal and vertical translations, rotation about the optical axis and scaling. The four degrees of freedom correspond to those of a similarity transformation, which is a particular case of homography transformations [25]. The image registration procedure follows two steps.

- First, an initialization is used to coarsely estimate large displacements. A correlation product in log-polar coordinates between the Fourier transforms of the reference image and

a deformed image provides the rotation angle and the scaling factor [26]. The horizontal and vertical translations are estimated using a correlation product in Cartesian coordinates. This coarse displacement estimation ensures the convergence of the next step.

- Second, a registration residual minimization is performed to measure with sub-pixel resolution the displacement amplitudes that minimize the  $L_2$ -norm of the registration residual over the fiducial/marker areas. This minimization follows an iterative scheme where a linear system is solved at each iteration. After each iteration, a new picture of the corrected image is generated by using the current estimation of the displacement field. Thanks to gray level interpolation schemes, sub-pixel resolutions are achieved [22]. The iterative procedure ends when the norm of the displacement amplitude corrections become less than  $10^{-3}$  pixel in the present case. At convergence, a registered image  $I_r(\mathbf{x} + \mathbf{u}(\mathbf{x}))$  is obtained.

More details on the implemented image registration algorithm can be found in Refs. [8,27]. This registration algorithm was chosen because it provided sub-pixel resolution on the displacement field estimation. In the present case, neither brightness nor contrast corrections were performed.

The image registration algorithm was applied to the whole image set described above. RMS residuals without any correction (*i.e.*,  $\rho(\mathbf{x}) = I_0(\mathbf{x}) - I_i(\mathbf{x})$ ) and after image registration (*i.e.*,  $\rho(\mathbf{x}) = I_0(\mathbf{x}) - I_r(\mathbf{x} + \mathbf{u}(\mathbf{x}))$ ) are shown as functions of image number in Fig. 4(a). The initial residual between images 0 to 19 was about 0.1 % of the dynamic range of the reference picture.

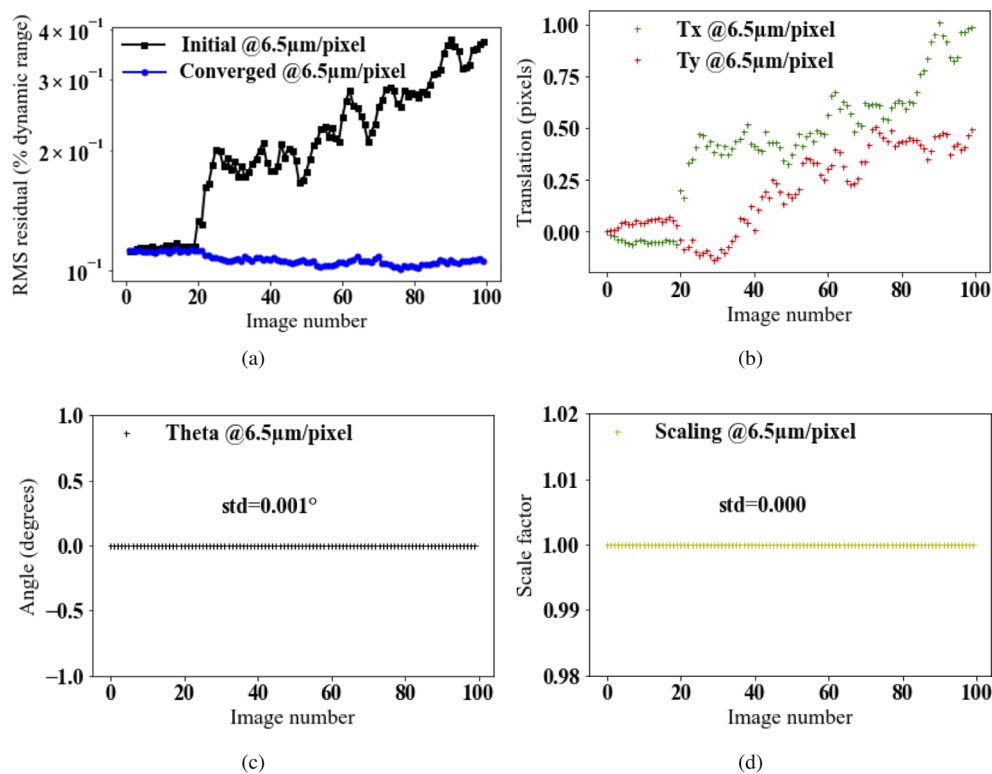


**Fig. 4.** Measurement results for the image set at high resolution (6.5 μm/pixel) to estimate uncertainties. (a) RMS residual between the reference image 0 and all images of the set before correction and after image registration. Measured translations (b), rotations (c) and scale factor (d) as functions of image number.



After image registration, the RMS residual was very close to this level. In the case with no prescribed displacement, the benefits of image registration were small (as expected). This result confirms that acquisition noise is about 0.1 % of the dynamic range.

When there were camera motions and automatic return between each acquisition (from images 20 to 99), the initial RMS residuals increased to reach a level up to 0.4 % of the dynamic range. This RMS change indicated that there was a difference between the reference image and the following ones. After spatial image registration, the RMS residual returned to the minimum level for images 1 to 99, thereby indicating that spatial registration was successful. The measured translations, rotation and scaling are plotted as functions of image number in Fig. 4(b-d). It is worth noting that non-zero displacement amplitudes were found not only for images 20 to 99 but also for images 1 to 19 for which no camera translations were prescribed. The measured displacements between each acquisition gave access to the measurement uncertainties associated with the whole optical setup and registration algorithm. The observed displacements were mainly due to translations since the rotation angle was equal to 0 on average with a standard deviation of  $0.001^\circ$ , and the scaling factor was equal to 1 with a negligible standard deviation. The measured translation amplitudes indicated that a drift occurred between the silica sample and the camera throughout the acquisition sequence. Image registration using digital image correlation principles made it possible to correct such displacement drift even if its amplitude was less than one pixel.

All these measurements indicate that the lowest RMS residual in this configuration was about 0.1 % of the dynamic range. Image changes that induce RMS residuals less than this threshold cannot be detected. It was also shown that the automatic return to the reference

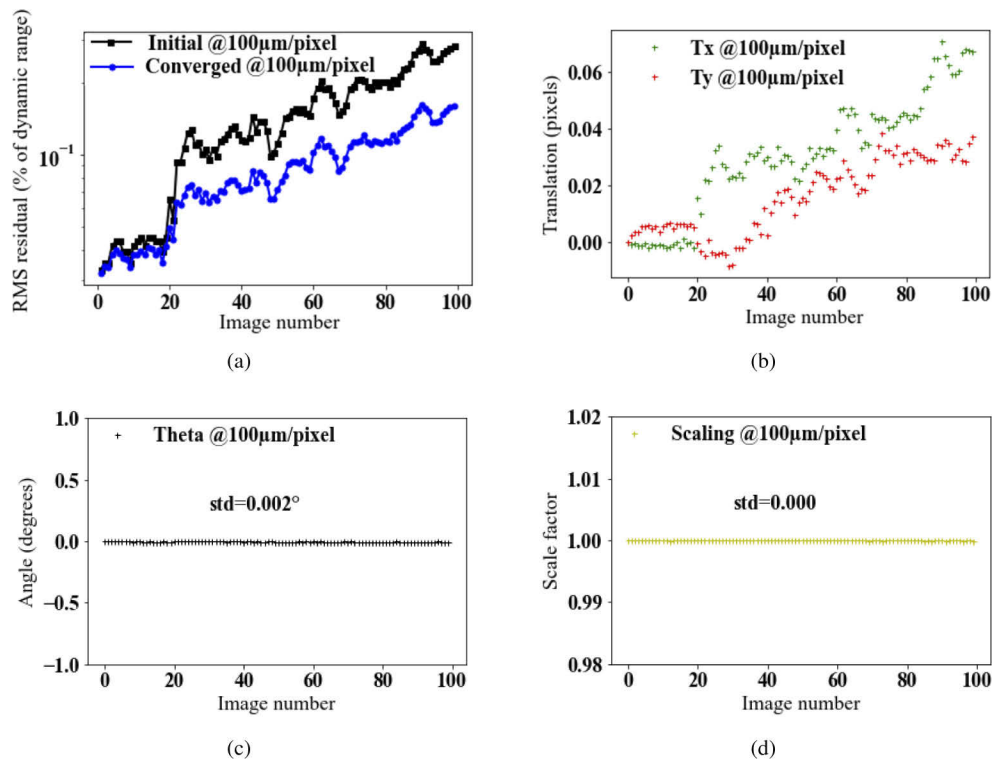


**Fig. 5.** Measurement results for the image set at low resolution (100 μm/pixel) to estimate uncertainties. (a) RMS residual between the reference image 0 and all images of the set before correction and after image registration. Measured translations (b), rotations (c) and scale factor (d) as functions of image number.

position corresponding to images 20 to 99 was not perfect. After 70 acquisitions without image registration, the displacement amplitude was greater than 1 pixel. To detect accurately damage initiation and growth in this configuration of the MELBA setup and consequently with the MDCC system, an efficient sub-pixel image registration method was needed to account for such small kinematic drifts [8].

In order to estimate the minimum reachable RMS residual at MDCC resolution (100  $\mu\text{m}/\text{pixel}$ ), a binning with a factor 15 was applied to the image set acquired at high resolution. Low resolution images were registered using the same registration code. At this resolution, the lowest RMS residual was ca. 0.02 % of the dynamic range (Fig. 5(a)). For images 20 to 99, the registrations lowered the residuals but their level did not reach that of acquisition noise. This difference was due to the pixel displacement amplitudes that became 15 times smaller for low resolution images than for high resolution images.

The measured displacements on low resolution images were in agreement with those obtained on high resolution images. Despite low resolution images, the translation and scale levels between acquisitions were well estimated (Fig. 5(b,d)). However, the measured rotation fluctuation at low resolution (Fig. 5(c)) was twice that at high resolution (Fig. 4(c)).

#### 4. Displacement corrections

In order to further check the effectiveness of the sub-pixel resolution of the registration algorithm, another image set was acquired with prescribed translations along the horizontal, vertical and longitudinal axis. Displacements between images were selected as follows:

- Images 0 to 9: Horizontal translation of 30  $\mu\text{m}$ .
- Images 10 to 19: Vertical translation of 40  $\mu\text{m}$ .
- Images 20 to 99: Longitudinal translation every 10 images. This displacement blurs images when longitudinal translations are greater than the depth of field.

The results of high resolution image registration are shown in Fig. 6. For this image set, the initial RMS residuals were greater than 1 % of the dynamic range. After registration of the first 30 images, the RMS residual was very close to the minimum level. For these images, the displacements were very well corrected and the registered images were nearly identical to the reference (up to acquisition noise). For the following images, the RMS residuals after registration were lower than their initial levels, but greater than the baseline. After each longitudinal displacement step, the residuals increased. The longitudinal displacement step was chosen to be about one half of the camera depth of field. As a consequence, the markers began to be blurred after image 30 when the depth of field was reached.

The measured translations for images 0 to 19 were consistent with the prescribed displacements. As rotations about the optical axis were not performed, the measured rotation angle was equal to 0 with a standard deviation of  $0.002^\circ$  (Fig. 6(c)), which is twice that reported earlier (Fig. 4(c)) for the same image resolution. This higher uncertainty in the rotation measurement appears to stem from the fact that the images used for the present study began to be blurred from image number 30 on. As the images became less sharp, the contrast of the markers used for image registration decreased. As a result, the accuracy of rotation measurements was reduced but was still low.

The measured scaling factor was equal to 1 before image 20 and increased every 10 images from images 20 to 99 (Fig. 6(d)). A consequence of prescribing longitudinal displacements was the measurement of horizontal and vertical translations (Fig. 6(b)). These motions were due to misalignment between the optical axis of the camera and the normal to the sample surface.

Displacements on low resolution images of this set were also measured. The estimated translations at high resolution are plotted as functions of those at low resolution in Fig. 7. The

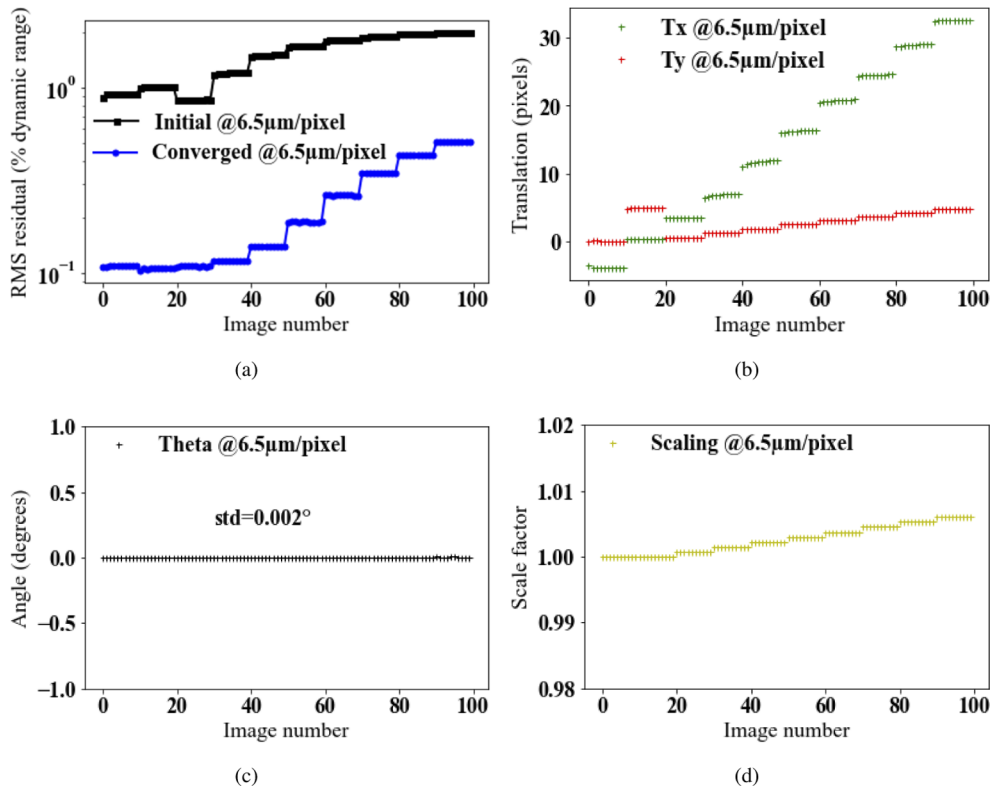


**Fig. 6.** Displacement measurements for an image set with a resolution of 6.5 μm/pixel. (a) RMS residuals before correction and after image registration. Measured translations (b), rotations (c) and scale factor (d) as functions of image number.

expected factor 15 between the two resolutions was nearly obtained (*i.e.*, 6.5 μm/pixel and 100 μm/pixel). Higher uncertainties were observed for *y* translations than for *x* translations between high and low resolutions due to smaller amplitudes in the *y*-direction. These results

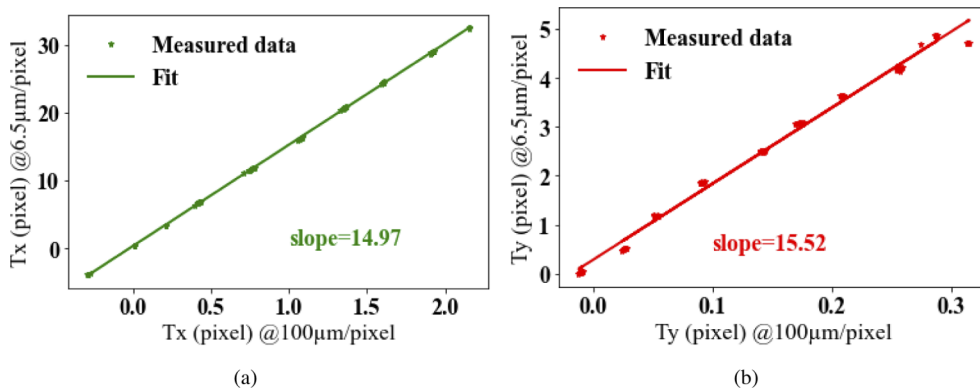


**Fig. 7.** Measured *x* (a) and *y* (b) translations at high resolution as functions of measured translations at low resolution. The measured slopes are about 15 as expected from the resolution change.

confirmed that the registration algorithm was effective to correct for displacements between images with sub-pixel resolution by performing the residual minimization on the four corners that contained markers.

## 5. Damage detection and quantification

In order to estimate the minimum diameter of damage sites that can be detected, a series of ultraviolet laser shots was performed on the fused silica sample. Images of the sample surface were acquired after each laser shot. Lighting conditions were the same as those used for the quantification of uncertainties. The reference image was that of the sample before the initiation shot. The acquisition procedure was the same as the sequence described previously (images 20 to 99), namely, an image of the sample surface was acquired, then the camera was moved to allow the laser to irradiate the sample. After each laser shot, an automatic return to the initial position was applied to the camera. A new image of the sample was acquired.

Between images 0 and 1, three (initiation) laser shots were performed to initiate 29 laser-induced damage sites. The damage diameter was estimated on high resolution (thresholded) images. The threshold was chosen to be slightly higher than the acquisition noise level (*i.e.*, 2 gray levels). The acquisition noise level is defined as the intensity fluctuation due to the acquisition system. The noise level for the high resolution images was estimated on a  $100 \times 100$ -pixel undamaged area in the reference image. The mean value was 0.95 gray level and its standard deviation 0.21 gray level. The equivalent diameter is that of a disk that has the same area as the damage site. Sixteen damage sites had an equivalent diameter less than  $50 \mu\text{m}$ , 10 sites an equivalent diameter ranging from  $50 \mu\text{m}$  to  $100 \mu\text{m}$ , and 3 sites an equivalent diameter greater than  $100 \mu\text{m}$ . After image 1, the laser beam was used for the growth sequence. The corresponding mean fluences are reported in Fig. 8. The fluence level was gradually increased to reach a maximum mean of about  $8 \text{ J/cm}^2$ , which is representative of fluences that may hit the final optics of high energy laser facilities [28].

### 5.1. Damage initiation

The RMS residuals at high and low image resolutions are shown in Fig. 8. The initial levels depended on displacement, damage initiation and growth, as well as acquisition noise. After image registration, the corresponding residual was no longer due to displacements but only to damage and acquisition noise. At the resolution of  $6.5 \mu\text{m}/\text{pixel}$ , the RMS residual corresponding to acquisition noise was 0.1 % of the dynamic range. After image registration, the RMS residual corresponding to the initially damaged sample was about 0.25 % of dynamic range at high and

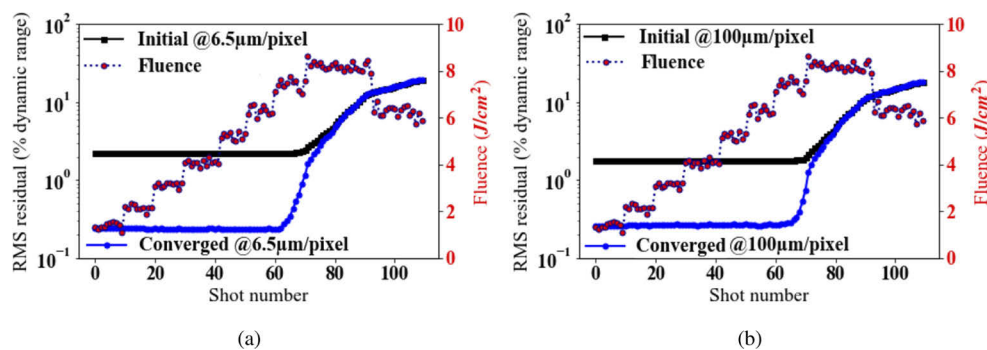


**Fig. 8.** Mean fluence of the shots inducing damage initiation and growth. RMS residuals obtained before and after image registration and laser beam fluence (a) at high resolution ( $6.5 \mu\text{m}/\text{pixel}$ ) and (b) low resolution ( $100 \mu\text{m}/\text{pixel}$ ).

low resolutions. This value was greater than the threshold corresponding to acquisition noise. The global residual indicated that the initiation sequence was detected at both resolutions.

Figure 9(a) shows the cumulative number of detected damage sites after initiation at high and low resolutions. The number at high resolution was considered as the reference. The smallest detected damage site at low resolution had an equivalent diameter of 53  $\mu\text{m}$ . When the diameter of a damage site was greater than 100  $\mu\text{m}$ , all initiated damage sites were detected at low resolution, whereas no damage site out of 16 was detected when its diameter was less than 50  $\mu\text{m}$ . When the diameter varied from 50  $\mu\text{m}$  to 100  $\mu\text{m}$ , 8 sites out of 10 were detected (Fig. 9(b)). The smallest diameter detectable at low resolution was about 50  $\mu\text{m}$ . This value is close to the detection performance announced to be at least 30  $\mu\text{m}$  for FODI [6].

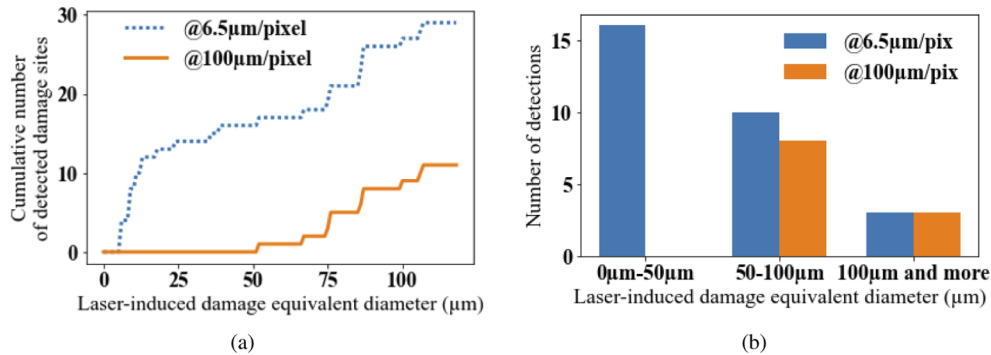


**Fig. 9.** (a) Cumulative number of initiated damage sites detected at high and low resolutions as function of damage site diameter. (b) Number of initiated damage sites detected at high and low resolutions as functions of damage site diameter.

## 5.2. Damage growth

Among the 29 initiated damage sites, 4 sites grew during the growth sequence (Fig. 10).

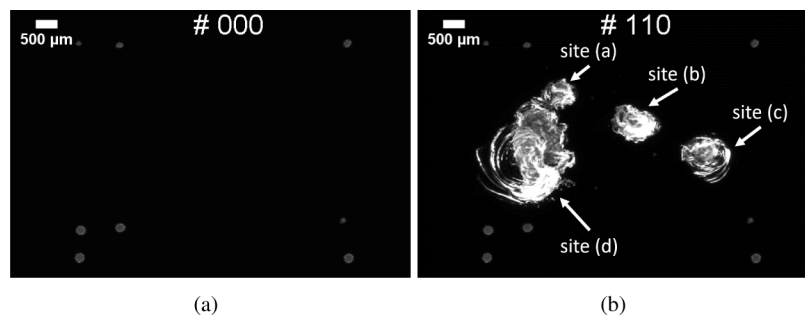


**Fig. 10.** Acquired images of the sample at high resolution (a) before damage growth (# 000) and (b) after the last laser shot (# 110). Four damage sites grew during the growth sequence (see [Visualization 1](#)).

The equivalent diameters of each growing site at low and high resolutions were measured (Fig. 11). The four damage sites grew after a different number of laser shots. It was observed that the diameters at high resolution related to damage growth before those at low resolution. The average delay of damage growth detection at high and low resolutions was about 1 laser shot for fluences varying between 6 and 8  $\text{J}/\text{cm}^2$ . In addition to this delay, the measured diameter at low resolution was overestimated compared to high resolution results for diameters less than

300  $\mu\text{m}$ . The growth rate at low resolution was different from that at high resolution since some false plateaus occurred.

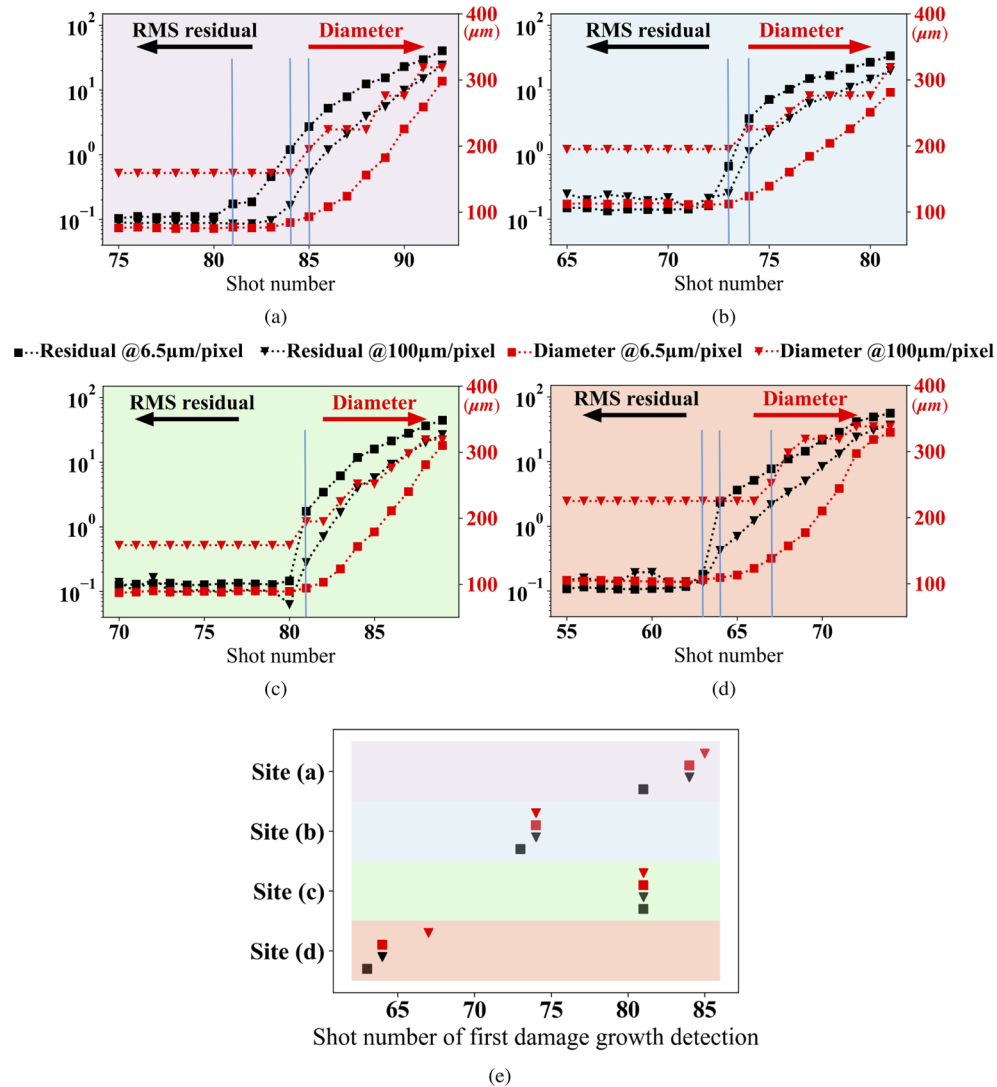


**Fig. 11.** RMS registration residual (% of dynamic range) measured on  $45 \times 45$ -pixel areas centered about the four growing damage sites (a-d) at high resolution (dotted black line with black square markers) and on the corresponding area at low resolution (dotted black line with black triangles) as functions of shot number. Changes of equivalent diameters (in  $\mu\text{m}$ ) of damage sites at high resolution (red dotted line with red square markers) and at low resolution (red dotted line with red triangles). The blue vertical lines indicate the first laser shot where damage growth was detected using each criterion. (e) Shot numbers of first damage growth detection for the four sites and for each growth indicator. The detection threshold for the measured diameters was a variation between two successive acquisitions greater than 6  $\mu\text{m}$ . For the RMS registration residuals, the detection threshold was a variation between two successive acquisitions greater than 0.1 % of dynamic range corresponding to acquisition noise.

The Pearson coefficient measures the correlation between two data sets [29,30]. This coefficient was assessed between the four growth indicators (*i.e.*, diameter at high and low image resolutions and registration residual at both resolutions) for the four growing damage sites. The correlation coefficient between the growth indicators was measured on the laser shot intervals shown in Fig. 11. These intervals were chosen to include the onset of damage growth. The Pearson correlation coefficient between low and high resolution diameters was equal to 0.927 on average for the four growing sites (Table 3). Thus the diameter at low resolution was not a perfect indicator for damage growth when the damage site was smaller than 300  $\mu\text{m}$  in diameter.

**Table 3. Pearson correlation coefficients measured between different indicators used to detect laser damage growth. The strongest correlation is between the measured damage diameter at 6.5  $\mu\text{m}/\text{pixel}$  and RMS residual at the same resolution. The lowest correlation is between measured damage diameters at 6.5  $\mu\text{m}/\text{pixel}$  and 100  $\mu\text{m}/\text{pixel}$  resolutions.**

Correlated quantities	Site (a)	Site (b)	Site (c)	Site (d)	Mean
<i>Diameter @6.5 <math>\mu\text{m}/\text{pixel}</math> and diameter @100 <math>\mu\text{m}/\text{pixel}</math></i>	0.873	0.933	0.967	0.933	<b>0.927</b>
<i>Diameter @6.5 <math>\mu\text{m}/\text{pixel}</math> and RMS residual @6.5 <math>\mu\text{m}/\text{pixel}</math></i>	0.995	0.997	0.998	0.995	<b>0.996</b>
<i>Diameter @6.5 <math>\mu\text{m}/\text{pixel}</math> and RMS residual @100 <math>\mu\text{m}/\text{pixel}</math></i>	0.959	0.989	0.976	0.968	<b>0.973</b>
<i>RMS residual @6.5 <math>\mu\text{m}/\text{pixel}</math> and RMS residual @100 <math>\mu\text{m}/\text{pixel}</math></i>	0.980	0.988	0.987	0.986	<b>0.985</b>

As images were registered, it was possible to analyze gray level variations of each pixel between each laser shot. The RMS residuals were measured on  $45 \times 45$ -pixel areas centered about each damage site at high resolution and on the corresponding  $3 \times 3$ -pixel areas at low resolution (Fig. 11). The Pearson correlation coefficient between measured diameters and RMS residuals at high resolution was equal to 0.996 on average (Table 3). This high level establishes a strong link between damage growth and high resolution RMS residuals. This value was not exactly one because RMS residuals contained not only damage information but also gray level variations of pixels belonging to a damage site. As shown in Fig. 11, damage growth was detected on RMS residuals at high resolution "1.25 laser shot" (on average) prior to similar detection at low resolution.

The Pearson coefficient between measured diameters at high resolution and RMS residuals at low resolution was about 0.973 (Table 3). This correlation level validates the link between damage growth and low resolution RMS residuals. The Pearson coefficient between low resolution RMS residuals and high resolution damage diameters was higher than that between low and high resolution damage diameters. It thus is better to use low resolution RMS residuals than low resolution damage diameters to detect efficiently damage growth. It is worth noting that there was no delay between the onset of damage growth observed on the measured diameters at high resolution and on the RMS residuals at low resolution. Hence, damage growth measurement via RMS residuals at low resolution was at least as effective as damage diameter measurement at high resolution.

The best indicator for damage growth between the four presented cases was the RMS residual at high resolution. With that indicator, it was possible to detect variations of damage diameters less than 9  $\mu\text{m}$  (Table 4). The smallest variations of damage diameter were provided for each growth indicator by calculating the damage variation measured with high resolution images at the laser shot where damage growth was observed with each indicator. The worst indicator was the measured diameter with the resolution of 100  $\mu\text{m}/\text{pixel}$ . The smallest damage variation

observable with this indicator was 15  $\mu\text{m}$ . The measured diameters at 6.5  $\mu\text{m}/\text{pixel}$  resolution were as efficient as the RMS residuals at 100  $\mu\text{m}/\text{pixel}$  with the smallest detectable damage diameter variation of 9  $\mu\text{m}$ .

**Table 4. Smallest diameter variation observed for each damage site with the measured diameter at 6.5  $\mu\text{m}/\text{pixel}$  and 100  $\mu\text{m}/\text{pixel}$ , the RMS residual at 6.5  $\mu\text{m}/\text{pixel}$  and 100  $\mu\text{m}/\text{pixel}$ .**

Damage growth indicator	Site (a)	Site (b)	Site (c)	Site (d)	Mean
<i>Diameter @6.5 <math>\mu\text{m}/\text{pixel}</math></i>	8 $\mu\text{m}$	11 $\mu\text{m}$	7 $\mu\text{m}$	8 $\mu\text{m}$	9 $\mu\text{m}$
<i>Diameter @100 <math>\mu\text{m}/\text{pixel}</math></i>	8 $\mu\text{m}$	11 $\mu\text{m}$	7 $\mu\text{m}$	34 $\mu\text{m}$	15 $\mu\text{m}$
<i>RMS residual @6.5 <math>\mu\text{m}/\text{pixel}</math></i>	<8 $\mu\text{m}$	<11 $\mu\text{m}$	<7 $\mu\text{m}$	<8 $\mu\text{m}$	<9 $\mu\text{m}$
<i>RMS residual @100 <math>\mu\text{m}/\text{pixel}</math></i>	8 $\mu\text{m}$	11 $\mu\text{m}$	7 $\mu\text{m}$	8 $\mu\text{m}$	9 $\mu\text{m}$

## 6. Conclusion

For the first time, a highly instrumented laser setup was used to quantify the effectiveness of a new damage growth indicator based on registration residual fields. This indicator probes the quality of sub-pixel image registration (*i.e.*, offsets to the gray level conservation). The displacement estimation used for this registration was sufficiently robust by using no more than 15% of the full image surface and a rather low contrast, which were well below what is classically encountered in digital image correlation applications.

Two image resolutions were compared to detect damage initiation and growth. High resolution images were used as ground truth. The low image resolution corresponded to those of imaging systems used in high energy laser facilities such as NIF, SG-III and LMJ. At low image resolution, it was shown that the smallest initiated damage site that could be detected using the RMS registration residual was about 50  $\mu\text{m}$  (*i.e.*, half of the image resolution). This value is close to the detection performance reported for FODI (at NIF).

Further, it was shown that the registration residual could be used as an efficient laser damage growth indicator since it outperformed the widely used diameter measurement at both resolutions. After image registration and using the registration residual as damage growth indicator, it was possible to detect 9  $\mu\text{m}$  damage diameter variations at the resolution of 100  $\mu\text{m}/\text{pixel}$ . This damage diameter variation was validated with the measurements at 6.5  $\mu\text{m}/\text{pixel}$  resolution, and with the RMS registration residuals at 100  $\mu\text{m}/\text{pixel}$  resolution. Yet, it was not detectable when measuring diameters at 100  $\mu\text{m}/\text{pixel}$  resolution.

These results pave the way toward a novel and more sensitive approach for detecting the initiation and growth of laser damage sites. The registration residuals were a powerful tool to capture the onset of damage growth in accordance with the needs of fusion scale high energy laser systems. The registration residual also provided improved resolution and allowed damage sites to be detected when smaller than the size of a single pixel of the imaging system. Even though applied to the monitoring of laser-induced damage, the proposed indicator may be utilized in other situations in which damage is suspected to occur.

**Acknowledgments.** The authors thank Jean-Yves Natoli, Nicolas Bonod and Sébastien Vermersch for useful and interesting discussions.

**Disclosures.** The authors declare no conflicts of interest.

**Data availability.** Data underlying the results presented in this paper are not publicly available at this time but may be obtained from the authors upon request.



## References

1. K. Manes, M. Spaeth, J. Adams, and M. Bowers, "Damage Mechanisms Avoided or Managed for NIF Large Optics," *Fusion Sci. Technol.* **69**(1), 146–249 (2016).
2. C. Lacombe, S. Vermersch, G. Hallo, M. Sozet, P. Fourtillan, R. Diaz, and J. Néauport, "Dealing with LMJ final optics damage: post-processing and models," in *Laser-induced Damage in Optical Materials 2020*, vol. 11514 C. W. Carr, V. E. Gruzdev, D. Ristau, and C. S. Menoni, eds., International Society for Optics and Photonics (SPIE, 2020).
3. P. Cormont, A. Bourgeade, S. Cavarro, T. Donval, T. Doualle, G. Gaborit, L. Lemaignere, and J.-L. Rullier, "Relevance of Carbon Dioxide Laser to Remove Scratches on Large Fused Silica Polished Optics," *Adv. Eng. Mater.* **17** 253–259 (2015).
4. T. Doualle, L. Gallais, S. Monneret, S. Bouillet, A. Bourgeade, C. Ameil, L. Lemaignère, and P. Cormont, "CO2 laser microprocessing for laser damage growth mitigation of fused silica optics," *Opt. Eng.* **56**(01), 1–9 (2016).
5. L. Mascio-Kegelmeyer, "Machine learning for managing damage on NIF optics," in *Laser-induced Damage in Optical Materials 2020*, vol. 11514 C. W. Carr, V. E. Gruzdev, D. Ristau, and C. S. Menoni, eds., International Society for Optics and Photonics (SPIE, 2020).
6. A. Conder, J. Chang, L. Kegelmeyer, M. Spaeth, and P. Whitman, "Final optics damage inspection (FODI) for the National Ignition Facility," in *Optics and Photonics for Information Processing IV*, vol. 7797 A. A. S. Awwal, K. M. Iftikharuddin, and S. C. Burkhart, eds., International Society for Optics and Photonics (SPIE, 2010), pp. 167–178.
7. F. Wei, F. Chen, B. Liu, Z. Peng, J. Tang, Q. Zhu, D. Hu, Y. Xiang, N. Liu, Z. Sun, and G. Liu, "Automatic classification of true and false laser-induced damage in large aperture optics," *Opt. Eng.* **57**(5), 1–11 (2018).
8. G. Hallo, C. Lacombe, J. Néauport, and F. Hild, "Detection and Tracking of Laser Damage Sites on Fused Silica Components by Digital Image Correlation," *Opt. Lasers Eng.* **146**, 106674 (2021).
9. L. Kegelmeyer, P. Fong, S. Glenn, and J. Liebman, "Local Area Signal-to-Noise Ratio (LASNR) algorithm for image segmentation," *Proc. SPIE* **6696**, 66962H (2007).
10. F. Bo, C. Fengdong, L. Bingguo, and L. Guodong, "Segmentation of small defects in Final Optics Damage Online Inspection images," in *2012 International Conference on Image Analysis and Signal Processing*, (2012), pp. 1–4.
11. M. A. Sutton, J.-J. Orteu, and H. W. Schreier, *Image Correlation for Shape, Motion and Deformation Measurements - Basic Concepts, Theory and Applications* (Springer Science, 2009).
12. F. Hild and S. Roux, "Digital Image Correlation," in *Optical Methods for Solid Mechanics. A Full-Field Approach*, P. Rastogi and E. Hack, eds. (Wiley-VCH, 2012), pp. 183–228.
13. P. Rastogi and E. Hack, *Optical Methods for Solid Mechanics: A Full-Field Approach* (Weinheim Wiley-VCH-Verl. 2012, 2012).
14. M. A. Sutton, "Computer Vision-Based, Noncontacting Deformation Measurements in Mechanics: A Generational Transformation," *Appl. Mech. Rev.* **65**(5), 050802 (2013).
15. F. Hild and S. Roux, *Handbook of Damage Mechanics* (Springer, 2015), chap. Evaluating Damage with Digital Image Correlation: A. Introductory Remarks and Detection of Physical Damage, pp. 1255–1275.
16. G. Z. Voyiadiis, *Handbook of Damage Mechanics* (Springer Science, 2015).
17. M. Veinhard, O. Bonville, R. Courchinoux, R. Parreault, J.-Y. Natoli, and L. Lemaignère, "MELBA: a fully customizable laser for damage experiments," in *Laser-Induced Damage in Optical Materials 2017*, vol. 10447 G. J. Exarhos, V. E. Gruzdev, J. A. Menapace, D. Ristau, and M. Soileau, eds., International Society for Optics and Photonics (SPIE, 2017), pp. 151–157.
18. M. Chambonneau and L. Lemaignere, "Multi-wavelength growth of nanosecond laser-induced surface damage on fused silica gratings," *Sci. Rep.* **8**(1), 891 (2018).
19. L. Lemaignère, M. Veinhard, F. Tournemene, C. Bouyer, R. Parreault, R. Courchinoux, J. Y. Natoli, C. Rouyer, and S. Bouillet, "A powerful tool for comparing different test procedures to measure the probability and density of laser induced damage on optical materials," *Rev. Sci. Instrum.* **90**(12), 125102 (2019).
20. L. Lemaignère, M. Veinhard, F. Tournemene, C. Bouyer, R. Parreault, R. Courchinoux, J.-Y. Natoli, C. Rouyer, and S. Bouillet, "Damage probability versus damage density: analysis from tests using small beams versus large beams," in *Laser-induced Damage in Optical Materials 2020*, vol. 11514 C. W. Carr, V. E. Gruzdev, D. Ristau, and C. S. Menoni, eds., International Society for Optics and Photonics (SPIE, 2020), pp. 1–15.
21. M. Veinhard, O. Bonville, S. Bouillet, R. Courchinoux, R. Parreault, J.-Y. Natoli, and L. Lemaignère, "Parametric study of laser-induced damage growth in fused silica optics with large beams at 351 nm. Part I: stochastic approach," *Appl. Opt.* **59**(31), 9643–9651 (2020).
22. F. Hild and S. Roux, "Comparison of local and global approaches to digital image correlation," *Exp. Mech.* **52**(9), 1503–1519 (2012).
23. L. Lemaignère, G. Dupuy, A. Bourgeade, A. Benoist, A. Roques, and R. Courchinoux, "Damage growth in fused silica optics at 351 nm: refined modeling of large-beam experiments," *Appl. Phys. B: Lasers Opt.* **114**(4), 517–526 (2014).
24. R. A. Negres, M. A. Norton, D. A. Cross, and C. W. Carr, "Growth behavior of laser-induced damage on fused silica optics under UV, ns laser irradiation," *Opt. Express* **18**(19), 19966–19976 (2010).
25. R. I. Hartley and A. Zisserman, *Multiple View Geometry in Computer Vision* (Cambridge University, 2004), 2nd ed.
26. B. S. Reddy and B. N. Chatterji, "An FFT-based technique for translation, rotation, and scale-invariant image registration," *IEEE Trans. on Image Process.* **5**(8), 1266–1271 (1996).

27. G. Hallo, C. Lacombe, J. Néauport, and F. Hild, "Detection and tracking of laser damage on LMJ vacuum windows by digital image correlation," in *Dimensional Optical Metrology and Inspection for Practical Applications X*, vol. 11732 K. G. Harding, S. Zhang, and B. Li, eds., International Society for Optics and Photonics (SPIE, 2021), pp. 87–95.
28. M. Nicolaizeau and J.-L. Miquel, "LMJ status: fifth bundle commissioning and PW class laser coupling," in *High Power Lasers for Fusion Research V*, vol. 10898 A. A. S. Awwal and C. L. Haefner, eds., International Society for Optics and Photonics (SPIE, 2019), pp. 1–10.
29. K. Pearson, "Notes on regression and inheritance in the case of two parents," *Proc. R. Soc. London* **58**(347-352), 240–242 (1895).
30. M. Nefzger and J. Drasgow, "The needless assumption of normality in pearson's r.," *Am. Psychol.* **12**(10), 623–625 (1957).